



# Defect-Rich Soft Carbon Porous Nanosheets for Fast and High-Capacity Sodium-Ion Storage

Xuhui Yao, Yajie Ke, Wenhao Ren, Xuanpeng Wang, Fangyu Xiong, Wei Yang, Mingsheng Qin, Qi Li,\* and Liqiang Mai\*

Soft carbon has attracted tremendous attention as an anode in rocking-chair batteries owing to its exceptional properties including low-cost, tunable interlayer distance, and favorable electronic conductivity. However, it fails to exhibit decent performance for sodium-ion storage owing to difficulties in the formation of sodium intercalation compounds. Here, microporous soft carbon nanosheets are developed via a microwave induced exfoliation strategy from a conventional soft carbon compound obtained by pyrolysis of 3,4,9,10-perylene tetracarboxylic dianhydride. The micropores and defects at the edges synergistically leads to enhanced kinetics and extra sodium-ion storage sites, which contribute to the capacity increase from 134 to 232 mAh g<sup>-1</sup> and a superior rate capability of 103 mAh g<sup>-1</sup> at 1000 mA g<sup>-1</sup> for sodium-ion storage. In addition, the capacitance-dominated sodium-ion storage mechanism is identified through the kinetics analysis. The in situ X-ray diffraction analyses are used to reveal that sodium ions intercalate into graphitic layers for the first time. Furthermore, the as-prepared nanosheets can also function as an outstanding anode for potassium-ion storage (reversible capacity of 291 mAh g<sup>-1</sup>) and dual-ion full cell (cell-level capacity of 61 mAh g<sup>-1</sup> and average working voltage of 4.2 V). These properties represent the potential of soft carbon for achieving high-energy, high-rate, and low-cost energy storage systems.

## 1. Introduction

The intermittent renewable energy resources such as tide, wind, and solar are hard to be used without sufficient large-scale energy storage systems.<sup>[1–3]</sup> The currently commercialized

X. Yao, Y. Ke, X. Wang, F. Xiong, W. Yang, M. Qin, Prof. Q. Li, Prof. L. Mai  
State Key Laboratory of Advanced Technology for Materials Synthesis  
and Processing

International School of Materials Science and Engineering  
Wuhan University of Technology  
Hubei, Wuhan 430070, China

E-mail: qi.li@whut.edu.cn; mlq518@whut.edu.cn

Dr. W. Ren

School of Chemistry

Faculty of Science

The University of New South Wales

Sydney, New South Wales 2052, Australia

The ORCID identification number(s) for the author(s) of this article  
can be found under <https://doi.org/10.1002/aenm.201803260>.

DOI: 10.1002/aenm.201803260

lithium-ion batteries (LIBs) cannot meet the increasing requirement of large-scale energy storage due to the limited and high cost of lithium resources.<sup>[4,5]</sup> Other alkali metals (especially sodium and potassium) are recognized as alternatives to lithium owing to abundance of elemental source and geographical distribution.<sup>[6–8]</sup> While the lithium and sodium share common properties as alkali metals, the assumption of adapting the same electrode materials from LIBs to sodium-ion batteries (SIBs) is not always efficacious.<sup>[9–11]</sup> The intrinsically higher redox potential of Na<sup>+</sup>/Na compared with Li<sup>+</sup>/Li (−2.71 > −3.04 V vs standard hydrogen electrode) and the sluggish Na<sup>+</sup> transport resulting from the larger radius of Na<sup>+</sup> compared with Li<sup>+</sup> (1.02 > 0.76 Å) directly affect the electrochemical performance.<sup>[10]</sup> As the most common anode for commercial LIBs, graphite exhibits superior reversible capacity (close to its theoretical capacity of 372 mAh g<sup>-1</sup>) as a result of consecutive migration of Li<sup>+</sup> between layered structures to forming LiC<sub>6</sub>.<sup>[12,13]</sup> Neverthe-

less, as demonstrated by previous reports, both the experiment carried out by Doeff et al.<sup>[14]</sup> and the theoretical calculation performed via Density Functional Theory studies by Wang et al.<sup>[15]</sup> in 2014 prove that it is hard to form sodium intercalated graphite compounds.<sup>[16,17]</sup> Only a small amount of Na<sup>+</sup> can be stored in graphite, leading to the suppressed reversible capacity of ≈30 mAh g<sup>-1</sup>.<sup>[11,18,19]</sup> In contrast to the graphite, the nongraphitizable hard carbon and graphitizable nongraphitic soft carbon have attracted most attentions as anodes for SIBs on account of their high capacity.<sup>[20,21]</sup> The sodiation of hard carbon at room temperature has been first reported by Stevens and Dahn,<sup>[22]</sup> achieving a capacity of ≈300 mAh g<sup>-1</sup>. A insertion–absorption process named as “house of cards” has been introduced at the same time and further proved by in situ small angle X-ray scattering study, which ascribes the sodiation to insertion of Na-ions and metallic adsorption (deposition) into the pores.<sup>[23,24]</sup> After that, other sodium storage mechanisms of hard carbon called “absorption-insertion” and “absorption-filling” have been introduced by Cao et al.<sup>[25]</sup> and Tarascon and co-workers,<sup>[26]</sup> respectively.<sup>[27]</sup> Considering the safety concern

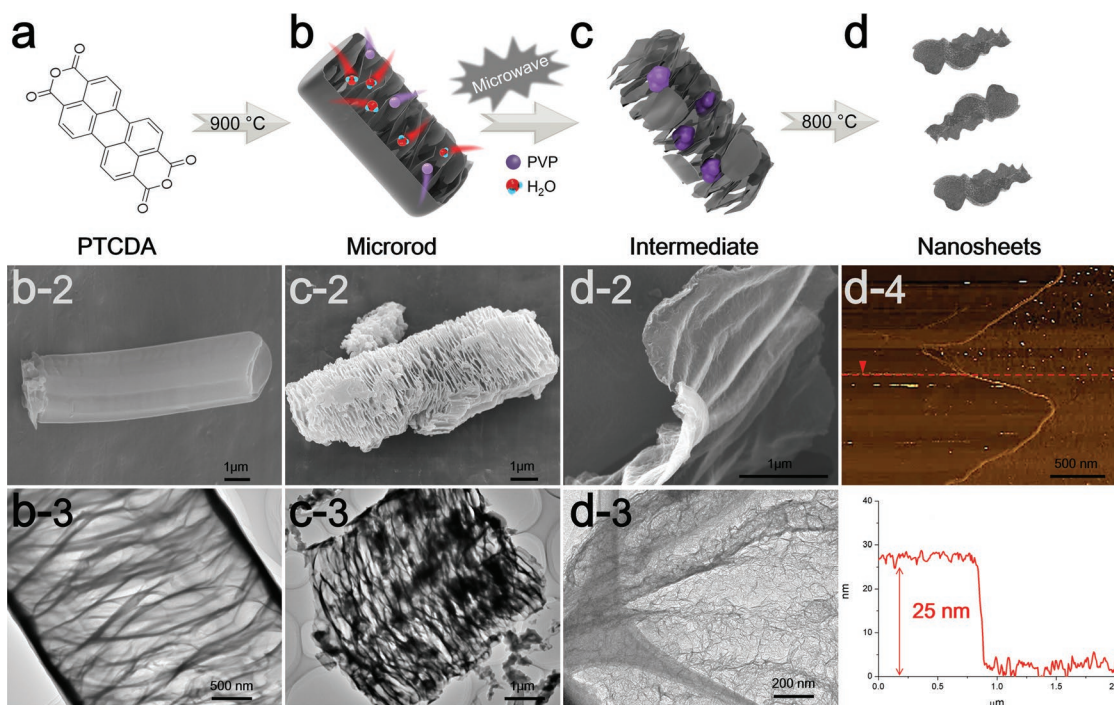


**Figure 1.** a–d) Schematic illustrations of the formation of the SC-NS materials. b-2) Scanning electron microscopy (SEM) and b-3) TEM images of SC-MR. c-2) SEM and c-3) TEM images of intermediate. d-2) SEM and d-3) TEM images of SC-NS. d-4) AFM results of SC-NS.

of the sodium dendrite formation arising from the very low potential plateau and the low ionic/electronic conductivity resulting from the tortuous atomic structure of hard carbon, the soft carbon is regarded as a feasible candidate for the SIB anode which has a higher electronic conductivity and tunable interlayer distance.<sup>[20,28]</sup> As demonstrated by Doeff et al., the petroleum coke derived soft carbon delivers a capacity of  $\approx 90 \text{ mAh g}^{-1}$  with the formation of  $\text{NaC}_{24}$ . However, it only works at  $86^\circ\text{C}$  because of the adoption of solid polymer electrolyte.<sup>[14]</sup> Recently, Song and co-workers synthesized mesoporous soft carbon by using a nano- $\text{CaCO}_3$  template method. Although the mesoporous soft carbon can achieve an initial capacity of  $331 \text{ mAh g}^{-1}$ , the reversible capacity only retains  $200 \text{ mAh g}^{-1}$  after 200 cycles.<sup>[29]</sup> Ji and co-workers reported an electrochemically expandable soft carbon with the specific capacity over  $200 \text{ mAh g}^{-1}$ .<sup>[20]</sup> Besides, pitch derived, mesitylene derived, carbon black derived carbons have also been investigated.<sup>[30–32]</sup> However, despite the decent performance of the above research, an energetic soft carbon anode which possesses both high capacity and fast charging has not been well explored and the  $\text{Na}^+$  storage mechanism also needs to be further investigated.

Fundamentally different from the diffusion-controlled process reacted in solid phase, the pseudocapacitive charge storage represents the faradaic charge-transfer reactions including solid fast ion intercalations and surface or subsurface redox reactions,<sup>[33,34]</sup> which has the advantage of fast charging/discharging rate leading to high power density.<sup>[33,35]</sup> Compared with the intrinsic pseudocapacitive materials (such as  $\text{MnO}_2$ ,  $\text{Nb}_2\text{O}_5$ , and  $\text{RuO}_2$ ) displaying the pseudocapacitance for a wide range of particle sizes, the capacitive characteristics of extrinsic materials only emerge through nanostructure by virtue of

maximizing reaction sites on the surface.<sup>[36]</sup> To the best of our knowledge, there is no previous report revealing the pseudocapacitive behaviors for soft carbon materials in SIBs which can accommodate fast and high-capacity sodium-ion storage.

Herein, we fabricated microporous soft carbon nanosheets (SC-NS) through microwave assisted exfoliating process. The as-prepared sample exhibits a higher capacity ( $232 \text{ mAh g}^{-1}$ ) and an outstanding rate performance ( $103 \text{ mAh g}^{-1}$  at  $1000 \text{ mA g}^{-1}$ ) compared with conventional soft carbon anodes. The sodium-ion storage mechanism of soft carbon nanosheets was revealed by in situ X-ray diffraction (XRD) technique and quantitative kinetics analysis, which indicates the boosted capacitive contribution. Beyond the sodium-ion storage, SC-NS also exhibits a specific capacity of 291 and  $117 \text{ mAh g}^{-1}$  at the current densities of 200 and  $2400 \text{ mA g}^{-1}$  as an anode for potassium-ion storage and can be employed as an efficient anode for dual-ion batteries (DIBs) with a cell-level capacity of  $61 \text{ mAh g}^{-1}$  and average working voltage of 4.2 V.

## 2. Results and Discussion

Schematic illustration of the step-by-step reactions and the morphological evolution of the soft carbon were demonstrated in Figure 1a–d. The SC-NSs were prepared from the conventional soft carbon microrod (SC-MR) originating from the pyrolysis of 3,4,9,10-perylene tetracarboxylic dianhydride (PTCDA) followed by the microwave-assisted exfoliated process. The choice of polyvinylpyrrolidone (PVP) is based on its ability to exfoliate and disperse carbon material such as graphite. Figure 1b-2 indicates that the SC-MR sample exhibits the morphology of

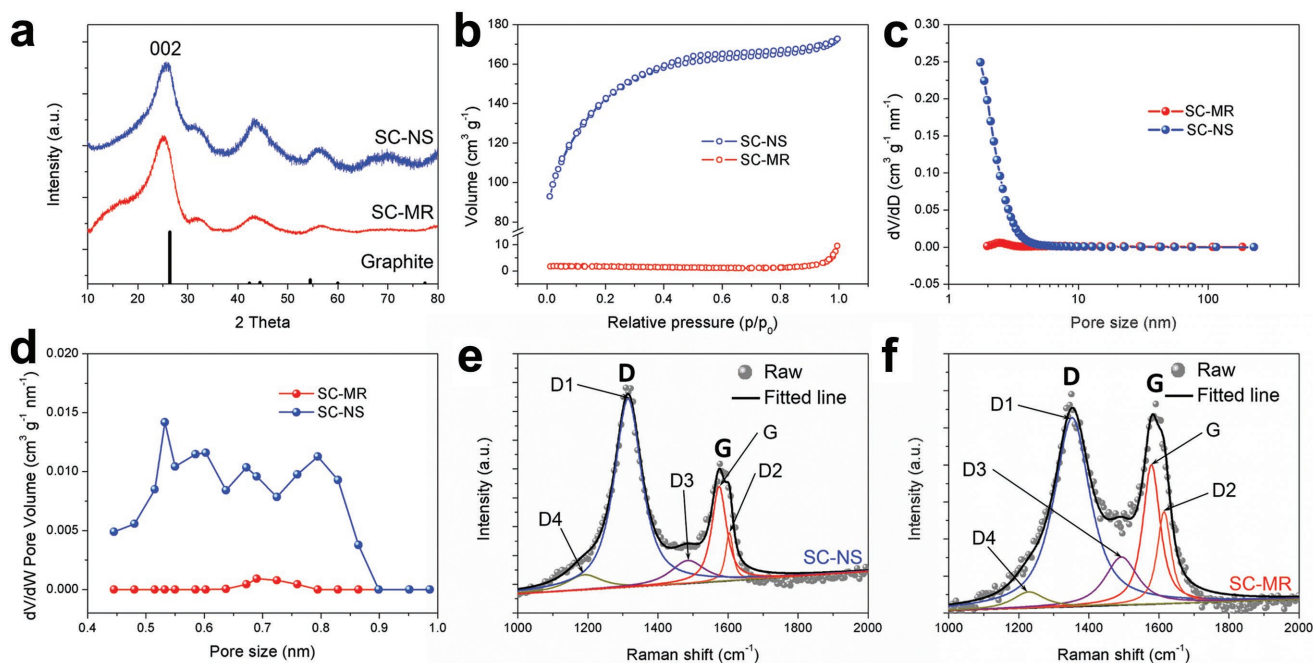


**Figure 2.** a) XRD pattern and b) nitrogen adsorption–desorption isotherms of SC-NS and SC-MR. Pore size distribution obtained from adsorption–desorption isotherms of c)  $N_2$  at 77 K and d)  $CO_2$  at 273 K. Raman spectra and curve fitting of e) SC-NS and f) SC-MR.

inerratic microrods, with the diameter of the microrods  $\approx 3 \mu\text{m}$ . Besides, the interior of the microrod is filled with hierarchical flakes (Figure 1b-3). The high-resolution transmission electron microscopy (HR-TEM) result displays the distorted lattice fringes of  $3.5 \text{ \AA}$  (Figure S1, Supporting Information), corresponding with the previous reports.<sup>[37,38]</sup> After the microwave treatment, the skin-layer of SC-MR is removed owing to the formation of “hotspot” (Figure 1c-2), which is attributed to the nonlinear heating rate originating from the intrinsic electromagnetic and thermal properties of materials, especially in the cavity structure.<sup>[39]</sup> The TEM result (Figure 1c-3) displays that the hollow space is filled with PVP. After the following pyrolysis process at  $800 \text{ }^\circ\text{C}$ , the volatile products (vinyl pyrrolidone) originating from the thermal degradation of PVP exfoliate the stacked hierarchical flakes (Figure S2, Supporting Information).<sup>[40]</sup> The final product SC-NS materials display a unique morphology of sheet-like nanostructure (Figure 1d-2) with a plicated surface (Figure 1d-3). The HR-TEM image shows that the both the nanosheet and nanorod soft carbon samples exhibit distorted lattice fringes of  $3.5 \text{ \AA}$  (Figure S1, Supporting Information). The thickness of SC-NS is  $\approx 25 \text{ nm}$ , which is proved by the atomic force microscope (AFM) results (Figure 1d-4).

The XRD patterns (Figure 2a) of both samples clearly exhibit a broad (002) diffraction peaks at around  $2\theta = 25.2^\circ$ , revealing a d-spacing of  $\approx 3.5 \text{ \AA}$ . The peak intensity of SC-NS is a bit higher than that of SC-MR, which is attributed to the second annealing process at  $800 \text{ }^\circ\text{C}$ . The nitrogen adsorption–desorption isotherms at 77 K are shown in Figure 2b, and the SC-NS sample exhibits the typical type-II isotherms with a H4-type hysteresis loop in the range of  $\approx 0.4\text{--}0.9 P/P_0$ , indicating the presence of abundant micropores and few mesopores (definition by International Union of Pure and Applied Chemistry).<sup>[41]</sup> The Brunauer–Emmerr–Teller surface areas of

the SC-NS and SC-MR samples are  $471.2$  and  $19.1 \text{ m}^2 \text{ g}^{-1}$ , respectively, implying a drastic increase (25 times) in the surface area which can enlarge the effective interface between electrode and electrolyte. The pore size distribution curves of two samples (Figure 2c) display that micropores of the size below  $3 \text{ nm}$  are dominated in the structure after the exfoliation process. It is known that the micropores play a positive role in carbon dioxide adsorption.<sup>[42,43]</sup> Therefore carbon dioxide adsorption–desorption isotherm was further investigated (Figure S3, Supporting Information) to accurately determine the micropore size distribution. The plots (Figure 2d) show a dramatic increase of micropore volume in the range of  $0.45\text{--}0.9 \text{ nm}$ . For the disordered material, the Raman spectrum is more useful than the diffraction techniques by virtue of its sensitivity in the short-range ordered structure. In Figure 2e,f, the Raman spectra are adopted to investigate the structural characteristics of the two samples. For the SC-MR sample, the intensity of D-band is comparable to the G-band. In contrast, the intensity ratio of  $I_D/I_G$  is estimated to be  $\approx 2$  for the SC-NS sample, indicating that there are more disordered structures in the SC-NS sample. Further, the D-band can be deconvoluted into four bands (Table S4, Supporting Information) by using a curve fitting in Gaussian–Lorentzian numerical simulation.<sup>[44]</sup> The increase of  $I_{D1}/I_G$  ratio from  $1.32$  to  $2.01$  after the exfoliation process indicates a significant improvement of D1 band derived from a vibration mode of carbon atoms at the graphene layer edges, which leads to extra sodium-ion storage sites.<sup>[16]</sup>

The sodium-ion storage performances of the two samples were first studied by using the cyclic voltammetry (CV) technique at a scan rate of  $0.1 \text{ mV s}^{-1}$  (Figure 3a). The SC-NS possesses a higher redox peak current and larger curve area compared with SC-MR, which indicates that the SC-NS has a faster kinetics property as well as higher specific capacity. As shown

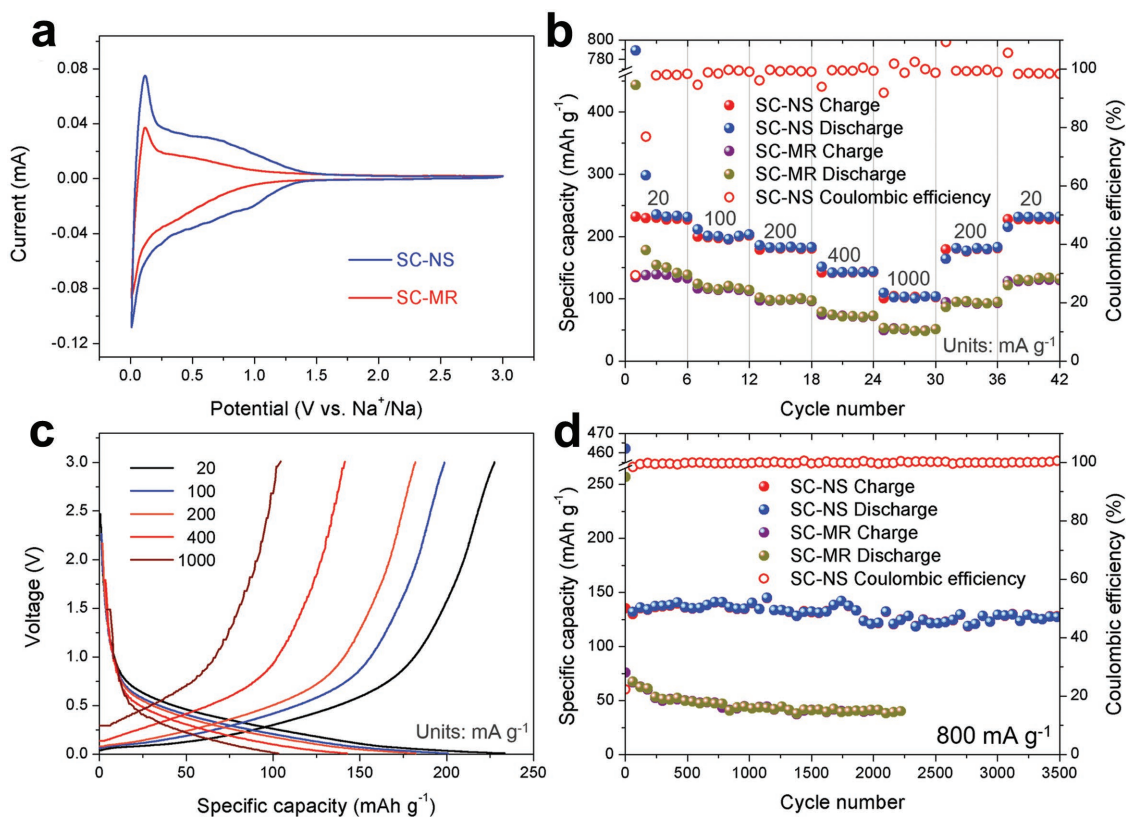


**Figure 3.** a) CV profiles, b) rate performance, c) corresponding charge–discharge curves, and d) long-term cycling capability of SC-NS and SC-MR samples.

in Figure 3b, the rate capabilities of two samples were evaluated at the current densities ranging from 20 to 1000 mA g<sup>-1</sup>. The SC-NS exhibits a reversible specific capacity of 232.2 mAh g<sup>-1</sup> at a current density of 20 mA g<sup>-1</sup>. When the current density increases to 1000 mA g<sup>-1</sup>, a specific capacity of 103.8 mAh g<sup>-1</sup> can still be achieved. Meanwhile, the capacity of 227.8 mAh g<sup>-1</sup> is retained after 40 cycles under a series of current densities, indicating an excellent structure stability. Whereas the SC-MR exhibits only 134.4 mAh g<sup>-1</sup> at 20 mA g<sup>-1</sup> and 48.3 mAh g<sup>-1</sup> at 1000 mA g<sup>-1</sup>. In addition, large initial irreversible capacities are observed for both SC-NS and SC-MR samples during the first cycle, owing to the decomposition of electrolyte, the formation of solid electrolyte interphase (SEI) on the surface, and the irreversible intercalation of sodium ions.<sup>[45]</sup> Formation of more SEI in SC-NS electrode is attributed to the enlarged surface area. The typical charge–discharge profiles of SC-NS at various current densities (Figure 3c) show that over 80% of the capacity is originated from the voltage range of 0.1–0.7 V versus Na<sup>+</sup>/Na. This potential plateau is more favorable as an anode than hard carbon (mainly below 0.1 V related to Na dendrite) in the matter of safety concern. The long-term cycling stabilities of these two samples (Figure 3d) were evaluated at a current density of 800 mA g<sup>-1</sup>. The reversible capacity of SC-NS maintains at 128.7 mAh g<sup>-1</sup> after 3500 cycles, corresponding to the outstanding capacity retention of 93%. In contrast, the SC-MR only exhibits an initial specific capacity of 87.5 mAh g<sup>-1</sup> and further decreases to 41.7 mAh g<sup>-1</sup> after 1500 cycles.

To further identify the sodium-ion storage process and discuss the transfer kinetics for the enhanced capacity and

rate performance, we performed CV tests under increasing voltammetric scan rates (range from 0.1 to 1 mV s<sup>-1</sup>, Figure S5, Supporting Information). Generally, the current response is a function of the sweep rate, which can be expressed as Equation (1)<sup>[46]</sup>

$$i(V) = av^b \quad (1)$$

where  $i$  is the current response at a certain voltage  $V$ ,  $v$  is the sweep rate,  $a$  and  $b$  are adjustable constants. When the value of  $b$  is 0.5, the current is proportional to  $v^{1/2}$ , which arises from a diffusion-controlled process. If the value of  $b$  is 1, the current is capacitance-controlled process and is linear to  $v$ . Figure 4a shows the log(scan rate)–log(current) plots at the voltages of 0.1, 0.35, and 1 V. The  $b$  values of SC-NS are calculated to range from 0.7 to 0.92, indicating that the capacitance-controlled process is more dominating in SC-NS compared with SC-MR (range from 0.58 to 0.77). These results are attributed to the unique nanosheet structure of SC-NS with abundant micropores. Furthermore, to further quantitatively differentiate the capacitive contribution from the capacity, Equation (2) proposed by Liu et al.<sup>[47]</sup> has been used.

$$i(V) = k_1v + k_2v^{1/2} \quad (2)$$

where  $k_1v$  stands for the capacitance-contribution and  $k_2v^{1/2}$  represents the contribution from the diffusion process. The diffusion process and capacitive effects can be distinguished through the linear plot of  $i/v^{1/2}$  versus  $v^{1/2}$ . Figure 4b shows the

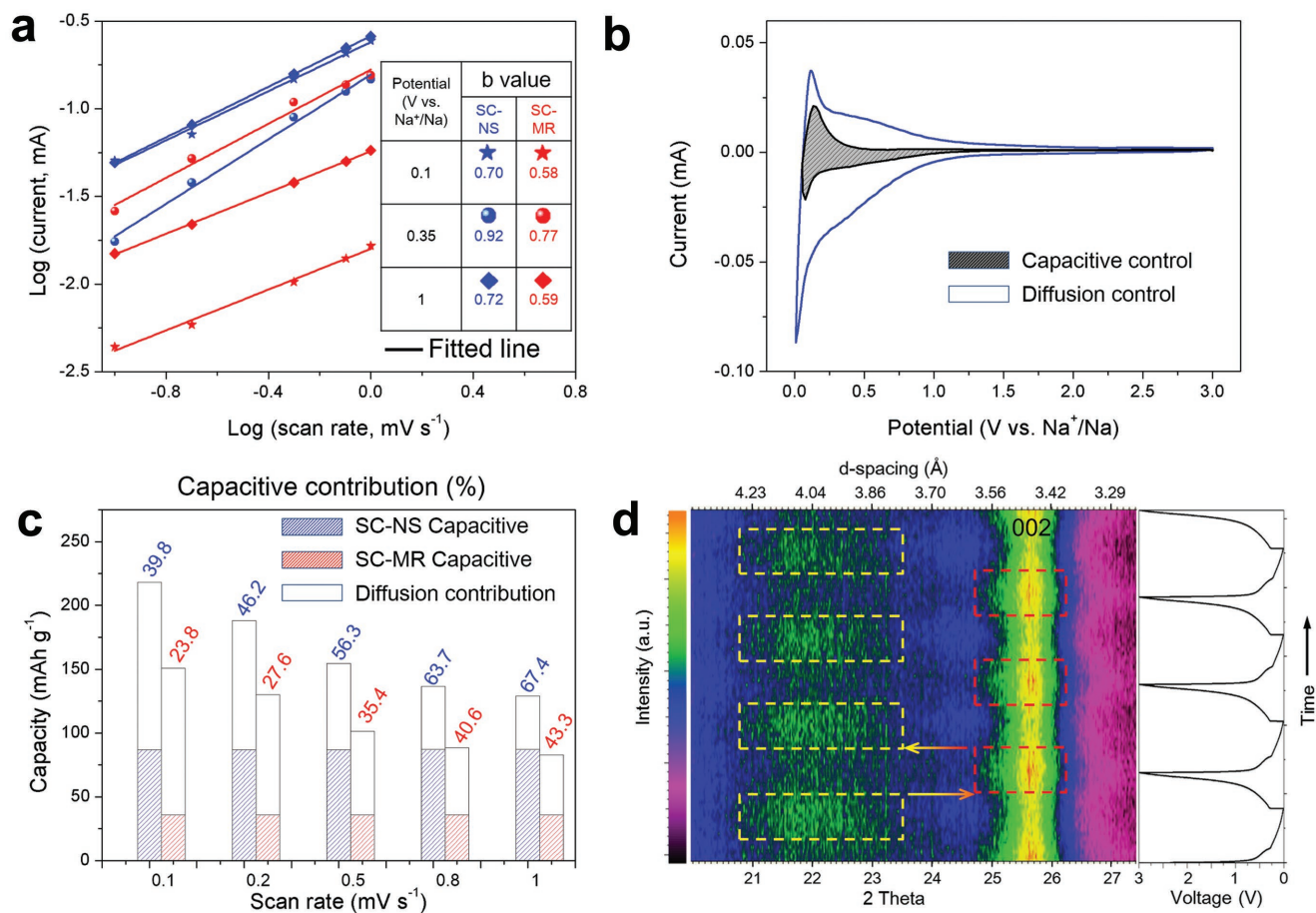


**Figure 4.** a) The calculated *b* values at the different potential of 0.1, 0.35, and 1 V. b) CV profile for SC-NS at a sweeping rate of 0.1 mV s<sup>-1</sup> and the estimated capacitive contribution (shaded region). c) The actual capacity contribution of capacitive (shaded region) and diffusion-controlled (blank region) of two samples at the different scan rate. d) The in situ XRD patterns with the time-potential curve under voltage windows of 0.01–3 V and corresponding *d*-spacing of SC-NS.

actual current response curve at a scan rate of 0.1 mV s<sup>-1</sup>, compared to the estimated capacitive contribution (shaded region, 39.8%). Figure 4c shows the total capacity, the capacity of capacitance (shaded region), and diffusion-controlled capacity (blank region) for the two samples at the different sweeping rates. The diffusion-controlled capacity of the SC-MR is comparable to that of the SC-NS, but the capacitance-controlled capacity of SC-NS is much higher than those of SC-MR. The galvanostatic intermittent titration technique (GITT) was adopted to reveal the diffusion coefficient of Na<sup>+</sup> (*D*<sub>Na</sub>) and to analyze the diffusion kinetics of the sodiated/desodiated process. The calculated diffusion coefficients *D*<sup>GITT</sup> for the two samples range from 10<sup>-10</sup> to 10<sup>-11</sup> cm<sup>2</sup> s<sup>-1</sup> (Figure S6, Supporting Information). To further check the above result, the diffusion coefficient on the basis of electrochemical impedance spectroscopy (*D*<sup>EIS</sup>) was calculated, which is consistent with the GITT results (Figure S7, Supporting Information). According to the equation:  $t \approx L^2/D$ , the diffusion time (*t*) is proportional to the square of diffusion length (*L*). A diffusion time of ≈0.2 s is estimated based on the ultrathin nanosheets compared with the ≈2000 s on the basis of the microrod architecture. Finally, the *I*-*V* transport measurements (Figure S8, Supporting Information) suggests that the SC-NS electrode has a modified charge transfer kinetics

compared with the SC-MR electrode, which could attribute to the better interconnection of sheets-like structure compared with rod-like structure.

In order to further investigate the sodium-ion storage mechanism, the in situ XRD technique has been utilized. As shown in Figure 4d, the broadband located at 25.6° appertain to the (002) plane. With the sodiation process to 0.01 V, the diffraction peak of (002) plane splits. A part of the peak remains at 25.6° and the other part of peak shifts directly from 25.6° to a bump of ≈21.7°, which corresponds well with the results Mitlin and co-workers reported earlier.<sup>[48,49]</sup> The remaining part of interlayer spacing indicates that there no sodium ions can intercalate into this part of the material, that is, it is inactive during sodiation. The fresh bump could be attributed to the expansion of the soft carbon structure during the sodiation process. Interestingly, the two disconnected diffraction peaks combine and restored at 25.6° after the desodiation process to 3.0 V, representing the recovery of the soft carbon structure after the deintercalation of sodium ions. Moreover, the shift of the diffraction peak in position and intensity is highly reversible in the following three cycles. According to the Bragg equation, the interlayer distance can be calculated from the diffraction peak. The interlayer distance of SC-NS sample increases from ≈3.5 to

$\approx 4.1$  Å after the intercalation of sodium ions. To investigate the structure transition clearly, the ex situ HR-TEM technique has been used (Figure S9, Supporting Information). Indeed, the lattice fringe also increases from 3.5 to  $\approx 4.1$  Å, corresponding well with the in situ XRD results.

In short, after the microwave assisted treatment, the deutero-genic micropores, nanoarchitecture, and increased defect concentration can be achieved simultaneously, which not only benefits enlarging the electrochemical reaction interface but also provides extra ion storage sites. Therefore, SC-NS electrodes show less concentration polarization and better electronic/ionic kinetics as reactions mostly occur on the surface and subsurface, hence leading to the enhanced rate performance. Given that only part of ions can intercalate into the interlayer, we conclude that the increased capacity is attributed to the extra storage sites originating from micropores and increased defect concentration.

In view of the outstanding sodium-ion storage performance of SC-NS, the all-carbon DIBs were also assembled by using the SC-NS as an anode and the commercial expanded graphite (EG) as a cathode (The morphology, structure characterization, and electrochemical performance of EG are shown in Figures S10 and S11, Supporting Information). The mechanism of the

DIBs is proposed in Figure 5a. In the typical charge process, the cations ( $\text{Na}^+$ ) and anions ( $\text{PF}_6^-$ ) are simultaneously inserted into SC-NS anode and EG cathode driven by applied voltage, respectively.<sup>[38,50]</sup> During the discharge process, the carrier will be deintercalated from the electrodes and return to the electrolyte for driving the circuit. Figure 5b shows the cell-level capacities (calculation based on the mass of both cathode and anode) of 61, 49, 38, 30, and 26  $\text{mAh g}^{-1}$  at a different current density of 100, 200, 400, 600, and 100  $\text{mA g}^{-1}$ , respectively. When the current density went back to 100 and 200  $\text{mA g}^{-1}$ , the discharge capacity of 55 and 46  $\text{mAh g}^{-1}$  were maintained, indicating a good rate reversibility. In addition, the DIBs can operate stably for over 350 cycles at the current density of 100  $\text{mA g}^{-1}$  (Figure 5c). The 350th discharge capacity is 56.6  $\text{mAh g}^{-1}$ , corresponding to a capacity retention of 94%. Figure 5d shows the typical voltage profiles of DIBs at different cycles. The average voltage is about 4.2 V, which is much higher than that of commercial LIBs (3.7 V). The energy density of DIBs is estimated to 256  $\text{Wh kg}^{-1}$ .

In addition, the electrochemical performances of SC-NS electrodes in potassium-ion battery (PIBs) have been further investigated. We perform the CV test on SC-NS electrode in a potential window of 0.01–3 V at a scan rate of

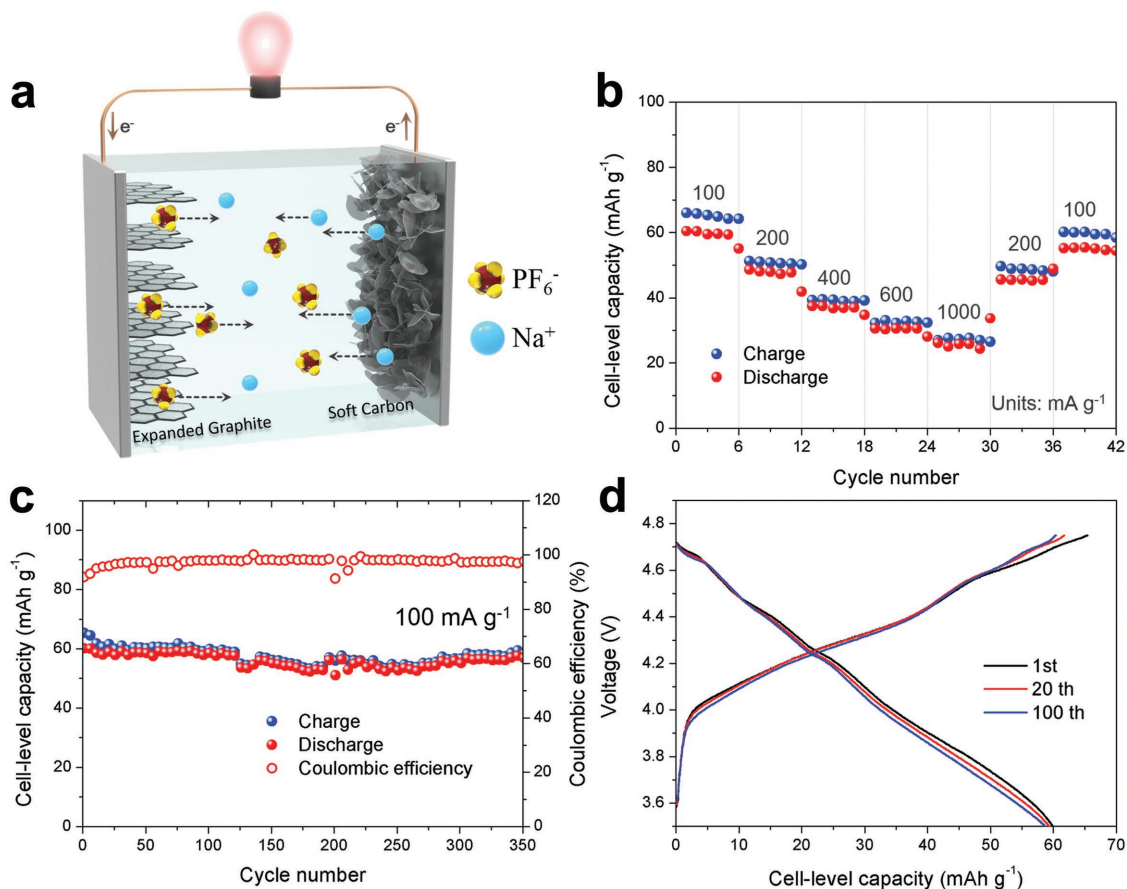


**Figure 5.** a) The schematic diagram, b) rate capability, c) cycling performance and corresponding d) charge–discharge curves of the soft carbon // expanded graphite dual-ion full battery.

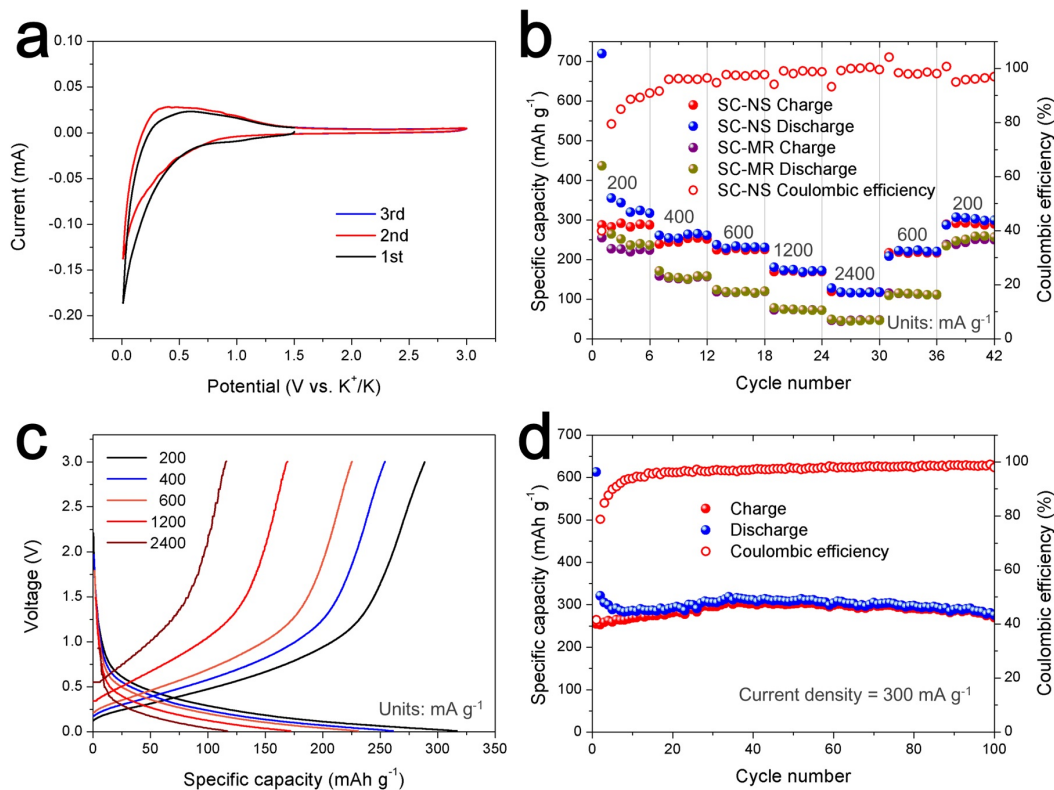


**Figure 6.** Potassium-ion battery performance: a) CV curves of SC-NS electrode at a scan rate of  $0.1 \text{ mV s}^{-1}$ . b) Rate performance of SC-NS and SC-MR electrodes and c) corresponding charge–discharge curves of SC-NS electrodes. d) Cycling capacity of SC-NS and SC-MR electrodes at a current density of  $300 \text{ mA g}^{-1}$ .

$0.1 \text{ mV s}^{-1}$  (Figure 6a). A broad pair of peaks at  $0.1\text{--}1 \text{ V}$  is clearly observed, which is related to the (de)intercalation of K ions. The initial irreversible capacity can be attributed to the K residual in the interlayer, the decomposition of electrolyte, and the formation of SEI. There is no obvious difference in the following two cycles, indicating a good reversibility. The SC-NS electrodes show the capacities of 291, 253, 228, 170, and  $117 \text{ mAh g}^{-1}$  at the current densities of 200, 400, 600, 1200, and  $2400 \text{ mA g}^{-1}$ , respectively (Figure 6b). When the current density is returned to  $200 \text{ mA g}^{-1}$ , the capacities of  $290 \text{ mAh g}^{-1}$  can be recovered, corresponding to the capacity retention of 99%. As a contrast, the SC-MR electrodes only exhibit the capacities of 254, 157, 119, 74, and  $47 \text{ mAh g}^{-1}$  at the corresponding current densities. The above results indicate that the unique micropores and nanoarchitecture of SC-NS after the treatment can lead to the better kinetics in PIBs. As shown in Figure 6c, the typical charge–discharge curves at different current density deliver a sloping voltage curves range of  $0.1\text{--}0.7 \text{ V}$  versus  $\text{K}^+/\text{K}$ . With the increase of current density, the overpotential increases gradually. Remarkably, the SC-NS electrodes exhibit less overpotential compared with SC-MR electrodes, especially at a high current density (Figure S12, Supporting Information). Figure 6d shows the cycling performance of PIBs at

the current density of  $300 \text{ mA g}^{-1}$ , indicating that almost the entire reversible capacity could be maintained after 100 cycles.

### 3. Conclusion

In summary, microporous SC-NSs have been successfully developed via a facile and easy-to-scale-up microwave-assisted exfoliating process. The structural analysis indicates significant improvements of surface area (from  $19.1$  to  $471.2 \text{ m}^2 \text{ g}^{-1}$ ), pore volume (more than 100 times) and favorable defects on graphene layer edges. Our kinetics analysis and in situ XRD test verify the capacitance-dominated sodium-ion storage mechanism. As the result of better electronic/ionic kinetics and extra storage sites, the SC-NS exhibits a high specific capacity ( $232 \text{ mAh g}^{-1}$ ) and excellent rate capability of  $103 \text{ mAh g}^{-1}$  at  $1000 \text{ mA g}^{-1}$  in sodium-ion storage. Furthermore, the SC-NS can also function as a high-performance anode for PIBs (reversible capacity of  $291 \text{ mAh g}^{-1}$  and outstanding rate capability of  $117 \text{ mAh g}^{-1}$  at current density of  $2400 \text{ mA g}^{-1}$ ) and DIBs (cell-level capacity of  $61 \text{ mAh g}^{-1}$  with an average voltage of  $4.2 \text{ V}$ ). Our strategy may bring a promising way of using soft carbon nanosheets for achieving high-energy and high-rate energy storage devices.

## 4. Experimental Section

**Synthesis of Microporous Soft Carbon Nanosheets:** The conventional soft carbon was prepared by directly pyrolysis of PTCDA (Alfa Aesar 98%) at 900 °C for 10 h under flowing argon atmosphere (5 °C min<sup>-1</sup>). Next, conventional soft carbon sample was added in 100 mL water with 10 wt% polyvinylpyrrolidone and the above mixture was sonicated at room temperature for 12 h. KOH (5 g) was added to the mixture and the solution was then further stirred at 60 °C for 2 h. Then, the sample was treated by using a microwave oven at an irradiation power of 300 W for 5 min. Next, the solid powder obtained was washed with 1 M HCl and deionized water several times to remove the remaining KOH and dried at 70 °C for 12 h. The dried powder was then annealed in a tube furnace from room temperature to 800 °C with a heating rate of 5 °C min<sup>-1</sup> under argon gas flow.

**Structural Characterization:** The morphology was observed by using the field emission scanning electron microscopy (JEOL JSM-7100F, acceleration voltage: 15 kV). The transmission electron microscopy (TEM) and high-resolution TEM were performed on a JEOL JEM-2100F microscope at 200 kV. The powder XRD and in situ XRD experiments were performed using Bruker D8 Discover X-ray diffractometer with a nonmonochromated Cu K<sub>α</sub> X-ray source. The surface area and pore-size distribution were calculated from N<sub>2</sub> adsorption isotherms and CO<sub>2</sub> adsorption isotherms measured by using a Tristar-3020 instrument. Atomic force microscope measurements were performed by Smart SPM 1000 (AIST-NT) with the aluminum coating n-type silicon probe (µmasch, HQ: NSC14/AIB5, 125 µm, 160 kHz, 5 N/M). The Raman spectra were recorded using a HORIBA LabRAM HR Evolution micro-Raman spectroscopy system.

**Electrochemical Measurements:** The electrochemical measurements were investigated with 2016 coin cells assembled in a glove box filled with argon atmosphere. The electrodes were made by mixing active materials, acetylene black, and polyvinylidene fluoride (7:2:1) in *N*-methylpyrrolidone solution. Then, the slurry was spread onto the Al foil and dried for at least 10 h at 70 °C. The mass loadings of the active material were 1.5–2 mg cm<sup>-2</sup>. For sodium-ion batteries, the electrolyte was 1 M NaPF<sub>6</sub> in ethyl carbonate, dimethyl carbonate, and ethyl–methyl carbonate with a mass ratio of 1:1:1. Counter electrode was Na metal. For potassium-ion batteries, the electrolyte was 1 M potassium bis (fluorosulfonyl) imide in a mixture of ethylene carbon/dimethyl carbonate (1:1 w/w). Counter electrode was K metal. The dual-ion full batteries were assembled by using expanded graphite as cathode and SC-NS as anode. The electrolyte was as same as the sodium-ion batteries. The Whatman glass microfiber filter (Grade GF/A) was used as the separator. The batteries were aged for at least 6 h to ensure sufficient infiltration of the electrolyte before testing. The cyclic voltammetry curves were obtained with the CHI1000D electrochemical workstation. Galvanostatic charge/discharge tests were cycled by using the LAND CT2001A multichannel battery testing system. The electrochemical impedance spectroscopy was evaluated by using an electrochemical workstation (Autolab PGSTAT302N). The cell-level capacity of the dual-ion battery was determined based on the total mass of the cathode and anode active materials according to the relationship as following Equation (3)<sup>[51,52]</sup>

$$C_{\text{total}} = \frac{C_a C_c}{C_a + C_c} \quad (3)$$

where the C<sub>total</sub>, C<sub>a</sub>, and C<sub>c</sub> stand for the capacity of dual-ion full cell, anode, and cathode, respectively.

## Supporting Information

Supporting Information is available from the Wiley Online Library or from the author.

## Acknowledgements

X.Y. and Y.K. contributed equally to this work. This work was supported by the National Natural Science Fund for Distinguished Young

Scholars (51425204), the National Natural Science Foundation of China (51832004, 21805219, and 51521001), the Programme of Introducing Talents of Discipline to Universities (B17034), the Yellow Crane Talent (Science and Technology) Program of Wuhan City, and the Fundamental Research Funds for the Central Universities (WUT: 2017IVA096, 2017111009, and 2017111040) the State Key Laboratory of Advanced Technology for Materials Synthesis and Processing (WUT: 2018-KF-1, 2018-KF-7). The authors thank Prof. Ali Javey of the University of California, Berkeley and Prof. Xudong Wang of the University of Wisconsin-Madison for strong support and stimulating discussions.

## Conflict of Interest

The authors declare no conflict of interest.

## Keywords

dual-ion full batteries, microwave, nanosheets, sodium/potassium-ion storage, soft carbon

Received: October 21, 2018

Revised: November 26, 2018

Published online:

- [1] P. Lu, Y. Sun, H. Xiang, X. Liang, Y. Yu, *Adv. Energy Mater.* **2018**, *8*, 1702434.
- [2] M. Z. Jacobson, M. A. Delucchi, *Energy Policy* **2011**, *39*, 1154.
- [3] X. Yao, Z. Zhu, Q. Li, X. Wang, X. Xu, J. Meng, W. Ren, X. Zhang, Y. Huang, L. Mai, *ACS Appl. Mater. Interfaces* **2018**, *10*, 10022.
- [4] Y. Jiang, Y. Wu, Y. Chen, Z. Qi, J. Shi, L. Gu, Y. Yu, *Small* **2018**, *14*, 1703471.
- [5] M. Wang, Z. Yang, W. Li, L. Gu, Y. Yu, *Small* **2016**, *12*, 2559.
- [6] P. Barpanda, G. Oyama, S. Nishimura, S. C. Chung, A. Yamada, *Nat. Commun.* **2014**, *5*, 4358.
- [7] M. D. Slater, D. Kim, E. Lee, C. S. Johnson, *Adv. Funct. Mater.* **2013**, *23*, 947.
- [8] S. Komaba, T. Hasegawa, M. Dahbi, K. Kubota, *Electrochem. Commun.* **2015**, *60*, 172.
- [9] J. W. Choi, D. Aurbach, *Nat. Rev. Mater.* **2016**, *1*, 16013.
- [10] N. Yabuuchi, K. Kubota, M. Dahbi, S. Komaba, *Chem. Rev.* **2014**, *114*, 11636.
- [11] S.-W. Kim, D.-H. Seo, X. Ma, G. Ceder, K. Kang, *Adv. Energy Mater.* **2012**, *2*, 710.
- [12] J. Jiang, J. R. Dahn, *Electrochim. Acta* **2004**, *49*, 4599.
- [13] K. Ozawa, *Solid State Ionics* **1994**, *69*, 212.
- [14] M. M. Doeff, Y. Ma, S. J. Visco, L. C. De Jonghe, *J. Electrochem. Soc.* **1993**, *140*, L169.
- [15] Z. Wang, S. M. Selbach, T. Grande, *RSC Adv.* **2014**, *4*, 4069.
- [16] Y. Okamoto, *J. Phys. Chem. C* **2014**, *118*, 16.
- [17] D. P. DiVincenzo, E. J. Mele, *Phys. Rev. B* **1985**, *32*, 2538.
- [18] J. Sangster, *J. Phase Equilib. Diffus.* **2007**, *28*, 571.
- [19] P. Ge, M. Foulletier, *Solid State Ionics* **1988**, *28–30*, 1172.
- [20] W. Luo, Z. Jian, Z. Xing, W. Wang, C. Bommier, M. M. Lerner, X. Ji, *ACS Cent. Sci.* **2015**, *1*, 516.
- [21] K. Tang, L. Fu, R. J. White, L. Yu, M.-M. Titirici, M. Antonietti, J. Maier, *Adv. Energy Mater.* **2012**, *2*, 873.
- [22] D. Stevens, J. Dahn, *J. Electrochem. Soc.* **2000**, *147*, 1271.
- [23] C. Bommier, D. Mitlin, X. Ji, *Prog. Mater. Sci.* **2018**, *97*, 170.
- [24] D. Stevens, J. Dahn, *J. Electrochem. Soc.* **2000**, *147*, 4428.
- [25] Y. Cao, L. Xiao, M. L. Sushko, W. Wang, B. Schwenzer, J. Xiao, Z. Nie, L. V. Saraf, Z. Yang, J. Liu, *Nano Lett.* **2012**, *12*, 3783.

- [26] B. Zhang, C. M. Ghimbeu, C. Laberty, C. Vix-Guterl, J. M. Tarascon, *Adv. Energy Mater.* **2016**, *6*, 1501588.
- [27] H. Hou, X. Qiu, W. Wei, Y. Zhang, X. Ji, *Adv. Energy Mater.* **2017**, *7*, 1602898.
- [28] Z. Jian, C. Bommier, L. Luo, Z. Li, W. Wang, C. Wang, P. A. Greaney, X. Ji, *Chem. Mater.* **2017**, *29*, 2314.
- [29] B. Cao, H. Liu, B. Xu, Y. Lei, X. Chen, H. Song, *J. Mater. Chem. A* **2016**, *4*, 6472.
- [30] D. A. Stevens, J. R. Dahn, *J. Electrochem. Soc.* **2001**, *148*, A803.
- [31] V. G. Pol, E. Lee, D. Zhou, F. Dogan, J. M. Calderon-Moreno, C. S. Johnson, *Electrochim. Acta* **2014**, *127*, 61.
- [32] R. Alcántara, J. M. Jiménez-Mateos, P. Lavela, J. L. Tirado, *Electrochem. Commun.* **2001**, *3*, 639.
- [33] V. Augustyn, P. Simon, B. Dunn, *Energy Environ. Sci.* **2014**, *7*, 1597.
- [34] V. Augustyn, J. Come, M. A. Lowe, J. W. Kim, P. L. Taberna, S. H. Tolbert, H. D. Abruna, P. Simon, B. Dunn, *Nat. Mater.* **2013**, *12*, 518.
- [35] T. Brezesinski, J. Wang, S. H. Tolbert, B. Dunn, *Nat. Mater.* **2010**, *9*, 146.
- [36] P. Simon, Y. Gogotsi, B. Dunn, *Science* **2014**, *343*, 1210.
- [37] X. Wang, K. Han, D. Qin, Q. Li, C. Wang, C. Niu, L. Mai, *Nanoscale* **2017**, *9*, 18216.
- [38] L. Fan, Q. Liu, S. Chen, Z. Xu, B. Lu, *Adv. Energy Mater.* **2017**, *7*, 1602778.
- [39] D. A. Jones, T. Lelyveld, S. Mavrofidis, S. Kingman, N. Miles, *Resour., Conserv. Recycl.* **2002**, *34*, 75.
- [40] M. I. Loría-Bastarrachea, W. Herrera-Kao, J. V. Cauich-Rodríguez, J. M. Cervantes-Uc, H. Vázquez-Torres, A. Ávila-Ortega, *J. Therm. Anal. Calorim.* **2011**, *104*, 737.
- [41] F. Barzegar, A. Bello, D. Momodu, M. J. Madito, J. Dangbegnon, N. Manyala, *J. Power Sources* **2016**, *309*, 245.
- [42] M. Sevilla, A. B. Fuertes, *Energy Environ. Sci.* **2011**, *4*, 1765.
- [43] X. Hu, M. Radosz, K. A. Cychosz, M. Thommes, *Environ. Sci. Technol.* **2011**, *45*, 7068.
- [44] A. Sadezky, H. Muckenhuber, H. Grothe, R. Niessner, U. Pöschl, *Carbon* **2005**, *43*, 1731.
- [45] E. M. Lotfabad, P. Kalisvaart, A. Kohandehghan, D. Karpuzov, D. Mitlin, *J. Mater. Chem. A* **2014**, *2*, 19685.
- [46] H. Lindström, S. Södergren, A. Solbrand, H. Rensmo, J. Hjelm, A. Hagfeldt, S.-E. Lindquist, *J. Phys. Chem. B* **1997**, *101*, 7717.
- [47] T. C. Liu, W. Pell, B. Conway, S. Roberson, *J. Electrochem. Soc.* **1998**, *145*, 1882.
- [48] J. Ding, H. Wang, Z. Li, A. Kohandehghan, K. Cui, Z. Xu, B. Zahiri, X. Tan, E. M. Lotfabad, B. C. Olsen, *ACS Nano* **2013**, *7*, 11004.
- [49] E. M. Lotfabad, J. Ding, K. Cui, A. Kohandehghan, W. P. Kalisvaart, M. Hazelton, D. Mitlin, *ACS Nano* **2014**, *8*, 7115.
- [50] S. Chen, J. Wang, L. Fan, R. Ma, E. Zhang, Q. Liu, B. Lu, *Adv. Energy Mater.* **2018**, *8*, 1800140.
- [51] M. Yoshio, S. Kugino, N. Dimov, *J. Power Sources* **2006**, *153*, 375.
- [52] U. Kasavajjula, C. Wang, A. J. Appleby, *J. Power Sources* **2007**, *163*, 1003.